

# Epitaxial growth and electronic properties of mixed valence $\text{YbAl}_3$ thin films

Shouvik Chatterjee,<sup>1</sup> Suk Hyun Sung,<sup>2</sup> David J. Baek,<sup>3</sup> Lena F. Kourkoutis,<sup>2,5</sup> Darrell G. Schlom,<sup>4,5</sup> and Kyle M. Shen<sup>1,5</sup>

<sup>1</sup>*Laboratory of Atomic and Solid State Physics, Department of Physics, Cornell University, Ithaca, New York 14853, USA*

<sup>2</sup>*School of Applied and Engineering Physics, Cornell University, Ithaca, New York 14853, USA*

<sup>3</sup>*School of Electrical and Computer Engineering, Cornell University, Ithaca, New York 14853, USA*

<sup>4</sup>*Department of Materials Science and Engineering, Cornell University, Ithaca, New York 14853, USA*

<sup>5</sup>*Kavli Institute at Cornell for Nanoscale Science, Ithaca, New York 14853, USA*

We report the growth of thin films of the mixed valence compound  $\text{YbAl}_3$  on  $\text{MgO}$  using molecular-beam epitaxy. Employing an aluminum buffer layer, epitaxial (001) films can be grown with sub-nm surface roughness. Using x-ray diffraction, *in situ* low-energy electron diffraction and aberration-corrected scanning transmission electron microscopy we establish that the films are ordered in the bulk as well as at the surface. Our films show a coherence temperature of 37 K, comparable to that reported for bulk single crystals. Photoelectron spectroscopy reveals contributions from both  $f^{13}$  and  $f^{12}$  final states establishing that  $\text{YbAl}_3$  is a mixed valence compound and shows the presence of a Kondo Resonance peak near the Fermi-level.

## I. INTRODUCTION

Intermetallic compounds containing certain rare-earth elements with an open  $f$ -shell, such as Yb, Ce, U, Eu, etc., in a periodic arrangement form the so-called Kondo lattice that exhibits a plethora of emergent exotic properties such as unconventional superconductivity,<sup>1</sup> quantum criticality,<sup>2</sup> hidden order,<sup>3</sup> and non-Fermi liquid behavior.<sup>4</sup> Understanding how these emergent properties arise from competing energy scales, and the possibility to rationally manipulate these interactions, is essential for any prospect of exploiting these properties for potential applications. Growing these intermetallics in epitaxial thin film form opens up new avenues for dimensional confinement and strain engineering of the Kondo lattice,<sup>5</sup> investigation of proximity effects,<sup>6</sup> and the creation of tunable electronic states via artificial superlattices.<sup>7</sup>

In intermetallic  $\text{YbAl}_3$ , the Yb valence fluctuates between two configurations,  $\text{Yb}^{2+}(f^{13})$  and  $\text{Yb}^{3+}(f^{12})$ .<sup>8</sup> Its ground state is non-magnetic and has a Kondo temperature of  $T_K \approx 670$  K. Transport and thermodynamic measurements indicate that there exists another low temperature scale,  $T^* \approx 34\text{K} - 40\text{K}$ , below which Fermi-Liquid-like behavior has been found to emerge.<sup>9</sup> Moreover, it undergoes a much slower crossover from the high temperature local moment regime to the low temperature Fermi liquid regime than predicted by the Single Impurity Anderson Model (SIAM).<sup>9,10</sup> These observations, along with the anomalies in the temperature-dependent soft x-ray photoemission spectroscopy measurements of bulk and Lu-doped single crystals, suggest that Kondo lattice effects play an important role.<sup>11,12</sup> The microscopic mechanism governing this behavior, however, remains enigmatic. One reason

is that  $\text{YbAl}_3$  does not naturally cleave, which has precluded measurements of its electronic structure by momentum-resolved techniques such as angle resolved photoemission spectroscopy (ARPES) and spectroscopic imaging scanning tunneling microscopy (SI-STM). Measurements of fractured or scraped single crystals are complicated by multiple crystallographic faces<sup>13</sup> and issues with surface quality, coupled with a propensity of the  $\text{YbAl}_3$  surface to form oxides.<sup>14</sup> One way of circumventing this difficulty is to synthesize epitaxial thin films and to measure them *in situ* with spectroscopic probes. Here, we report the first progress along this direction.

## II. EXPERIMENTAL DETAILS

Thin films were grown on  $\text{MgO}$  substrates in a Veeco GEN10 MBE system with a liquid nitrogen cooled cryoshroud with a base pressure below  $2 \times 10^{-9}$  torr. Prior to growth,  $\text{MgO}$  substrates were annealed in vacuum for 20 minutes at  $800^\circ\text{C}$ . Epitaxial (001)  $\text{YbAl}_3$  films were achieved by first depositing a 1 - 2 nm thick aluminum buffer layer, followed by a  $\text{LuAl}_3$  buffer layer on which  $\text{YbAl}_3$  was grown. For the deposition of the  $\text{LuAl}_3$  and  $\text{YbAl}_3$ , elements were co-deposited onto a rotating substrate from Langmuir effusion cells at a growth rate of  $\approx 0.4$  nm/min. During growth *in situ* reflection high-energy electron diffraction (RHEED) was used to monitor the surface evolution. After growth, the films were immediately transferred under ultra-high vacuum ( $5 \times 10^{-10}$  torr) into an analysis chamber where low-energy electron diffraction (LEED) and *in situ* photoemission spectroscopy were performed. Bulk structural characterization was performed *ex situ* by four-circle x-ray diffraction (XRD) using  $\text{Cu K}_\alpha$  radiation. The atomic scale structure of the  $\text{YbAl}_3$

thin film was studied by aberration-corrected scanning transmission electron microscopy (STEM) and electron energy loss spectroscopy (EELS) performed on a FEI Titan Themis 300. Cross-sectional TEM specimen were prepared using a FEI Strata 400 Focussed Ion Beam with a final milling step of 2 KeV to reduce surface damage. Films were further characterized by atomic force microscopy (AFM), scanning electron microscopy (SEM) and resistivity measurements.

### III. RESULTS AND DISCUSSION

Both  $\text{YbAl}_3$  and its structural analogue  $\text{LuAl}_3$  crystallize in a cubic  $\text{AuCu}_3$  (L12) structure where Yb/Lu atoms occupy the vertices of the unit cell and Al atoms occupy the face-centered positions (Fig. 1(c)). Various compounds belonging to the same space group, such as  $\text{AuCu}_3$  have been reported to show an order-disorder transition, where above a certain temperature the disordered face-centered cubic (FCC) phase is stabilized.<sup>15</sup> In the disordered FCC phase occupation probability of all the lattice sites becomes  $\frac{1}{4}$  for Yb/Lu and  $\frac{3}{4}$  for Al atoms. Diffraction measurements can distinguish the cubic ordered phase, as its diffraction peaks should be observed for all values of  $h, k, \ell$  indices, while for the disordered phase, the structure factor becomes zero when indices are mixed between odd and even  $h, k, \ell$  indices.  $\text{YbAl}_3$  and  $\text{LuAl}_3$  have lattice constants of  $a = 4.2 \text{ \AA}$  and  $a = 4.19 \text{ \AA}$ , respectively. The lattice constants of MgO and aluminum are  $4.21 \text{ \AA}$  and  $4.05 \text{ \AA}$ , respectively, which provide a good lattice match to the  $\text{LuAl}_3$  or  $\text{YbAl}_3$  film. MgO and Al have a different space group ( $Fm\bar{3}m$ ) than that of ordered  $\text{YbAl}_3/\text{LuAl}_3$  ( $Pm\bar{3}m$ ), but the surface atomic arrangement of the oxygen atoms on the (001) surface of MgO and the Al atoms on the Aluminum (001) surface provide an excellent template for the epitaxial integration of  $\text{YbAl}_3/\text{LuAl}_3$  on MgO substrates with aluminum as a buffer layer (Figs. 1(a)-(c)). The face-centered sites and vertices are inequivalent for ( $Pm\bar{3}m$ ) and thus, the  $\text{LuAl}_3/\text{YbAl}_3$  layers can nucleate either where the  $\text{LuAl}_3/\text{YbAl}_3$  is in perfect registry with that of the Al unit cell (left domain in Fig. 1(d)) or where it is shifted by  $(\frac{1}{2}, \frac{1}{2}, 0)$  (right domain in Fig. 1(d)) leading to the formation of anti-phase domains (Fig. 1(d)). Our EELS map confirm that there is negligible inter-diffusion across the boundary between the  $\text{YbAl}_3$  and  $\text{LuAl}_3$  layers (Fig. 1(e)).

In Fig. 2(a), we show an out-of-plane  $\theta$ - $2\theta$  XRD scan. Prominent 001 and 003 Bragg peaks can be easily identified, confirming the films have the ordered L12 structure.<sup>16</sup> Moreover, the observation of only 00 $\ell$  film peaks establishes that our films are single phase with the desired (001)  $\text{YbAl}_3$  out-of-plane orientation. An analysis of the peak positions reveal that the  $\text{LuAl}_3$  layer is

relaxed while  $\text{YbAl}_3$  is strained to the underlying  $\text{LuAl}_3$  layer. An azimuthal  $\phi$  scan of the (110)  $\text{YbAl}_3$  film peak is shown in Fig. 2(b). The  $\phi$  scan in combination with the  $\theta$  -  $2\theta$  scans establishes the epitaxial relationship of  $\text{YbAl}_3/\text{LuAl}_3$  with respect to MgO where (001)[100]  $\text{YbAl}_3/\text{LuAl}_3 \parallel (001)[100]$  MgO. Rocking curve measurements were performed on the 001 film peak and the 002 substrate peak, shown in Fig.2 (c). The full width at half maximum (FWHM) of the the film peak was found to be 0.32 degrees while that for the substrate peak was 0.03 degrees.

The growth process was initiated first by depositing an aluminum buffer layer at a substrate temperature of  $500^\circ\text{C}$ . RHEED patterns taken after the deposition process shown in Fig. 3(b) reveal large transmission spots indicative of 3D grains. Although depositing aluminum at elevated temperatures results in a rough surface, it also nucleates epitaxially oriented grains providing a template for the growth of epitaxially oriented  $\text{YbAl}_3/\text{LuAl}_3$  layers. Growing  $\text{YbAl}_3/\text{LuAl}_3$  directly on MgO or depositing the Al buffer layer at a lower temperature resulted in a mixed orientation where a secondary orientation with (111)  $\text{YbAl}_3/\text{LuAl}_3 \parallel (001)$  MgO was observed. Films grown directly on MgO were also found to be much rougher by AFM, as  $\text{YbAl}_3/\text{LuAl}_3$  layers do not wet the MgO (001) surface well. Subsequently, a second buffer layer of  $\text{LuAl}_3$  was deposited at a substrate temperature of  $200^\circ\text{C}$  and annealed in vacuum at  $350^\circ\text{C}$  for 30 minutes. The deposition of the  $\text{LuAl}_3$  buffer layer was also important to achieve epitaxial  $\text{YbAl}_3$  films, as growing  $\text{YbAl}_3$  directly on the aluminum buffer layer resulted in secondary phases. As the  $\text{LuAl}_3$  growth proceeded, the RHEED pattern became more and more two-dimensional as individual grains coalesced into a flat surface (Fig. 3(d)). Thicker  $\text{LuAl}_3$  buffer layers and post-annealing resulted in better quality films. Finally, the sample was cooled down to  $200^\circ\text{C}$  for the deposition of the  $\text{YbAl}_3$  layer. The growth temperature was ramped up to  $315^\circ\text{C}$  after initiating growth at  $200^\circ\text{C}$ . During growth, half-order peaks can be seen in RHEED images taken along the [100] azimuth (Fig. 3(e)), indicating that the  $\text{YbAl}_3$  film grows with the ordered L12 structure (Fig. 1(c)).

*In situ* LEED patterns (Fig. 4(a)) indicate that the surface of the films is ordered with no additional surface reconstruction. The smoothness of the films was confirmed by AFM measurements (Fig. 4(b)) revealing a smooth surface with an rms roughness of only  $\approx 1.8 \text{ \AA}$  over a  $1 \mu\text{m}$  by  $1 \mu\text{m}$  field of view. SEM and corresponding energy dispersive x-ray spectroscopy (EDX) measurements on a 35 nm thick  $\text{LuAl}_3$  film with a 1.2 nm aluminium buffer shown in (Figs. 4(c)-(d)) reveal small aluminium-rich regions where excess aluminium has precipitated out. This observation is in agreement with the Yb-Al phase diagram (at temperatures relevant to our study a two-phase Al +  $\text{YbAl}_3$  region exists).<sup>17</sup> The expulsion of excess aluminium from the film ensures

robustness of the growth method against slight flux mismatch, ensuring correct stoichiometry of our films.

Having investigated the structural aspects of our thin films, we now turn to their electronic properties. Four-point resistivity measurements were performed in a van der Pauw geometry using both a home-built dipper setup and a Quantum Design PPMS system. The temperature-dependent resistivity for a 20 nm YbAl<sub>3</sub>/1.6 nm LuAl<sub>3</sub>/1.2 nm Al and 35 nm LuAl<sub>3</sub>/1.2 nm Al thin films are shown in Figs. 5(a) and 5(b), respectively. The resistivity curves are found to be qualitatively similar to that obtained for corresponding single crystals.<sup>18</sup> The resistivity of YbAl<sub>3</sub> is plotted as a function of  $T^2$  in the inset of Fig. 5(a), which shows that the film deviates from  $T^2$  Fermi liquid behavior ( $\rho(T) = \rho_0 + AT^2$ ) above  $T^* \approx 37$  K, similar to single crystals,<sup>9</sup> albeit with a lower residual resistivity for the single crystals. The roughness of the aluminum buffer layer employed at the beginning of the growth process and the presence of anti-phase domain boundaries could be potential contributors to both the higher residual resistivity and wide rocking curves (Fig. 2(c)) of our thin films. The  $T^2$  coefficient of resistivity in our thin films is  $A = 6 \times 10^{-4} \pm 1 \times 10^{-4} \mu\Omega \text{ cm/K}^2$  similar to the earlier reported values for single crystals.<sup>19,20</sup> Assuming a similar value of  $\gamma = 45 \text{ mJ/mol K}^2$  in our thin films as in single crystals, we obtain a Kadowaki Woods ratio ( $A/\gamma^2$ ) of  $\approx 3 \times 10^{-7} \mu\Omega \text{ cm mol}^2 \text{ K}^2/\text{mJ}^2$ , which is orders of magnitude lower than the universal behavior observed in many  $f$  electron systems,  $A/\gamma^2 = 1 \times 10^{-5} \mu\Omega \text{ cm mol}^2 \text{ K}^2/\text{mJ}^2$ .<sup>21</sup> This apparent discrepancy can be reconciled by incorporating corrections due to the large degeneracy ( $N = 8$ ) of the Yb  $4f$   $J = 7/2$  in the ground state that gives a value of  $A/\gamma^2 = 3.6 \times 10^{-7} \mu\Omega \text{ cm mol}^2 \text{ K}^2/\text{mJ}^2$ .<sup>22</sup>

Finally, Fig. 6 shows *in situ* photoemission spectra (PES) at normal emission obtained from these films. All measurements were taken using a monochromatized VUV5000 helium discharge lamp using a photon energy of 21.2 eV and a Scienta R4000 analyzer in a UHV chamber with base pressure better than  $5 \times 10^{-11}$  torr. The observed spectra show two sets of characteristic features corresponding to  $f^{13}$  and  $f^{12}$  final states, respectively, indicative of YbAl<sub>3</sub> being a mixed valence compound. This is again consistent with earlier measurements of YbAl<sub>3</sub> single crystals.<sup>11,23</sup> Spectral peaks very close to the Fermi level with a binding energy of 0.03 eV and 1.34 eV, respectively, constitute features derived from Yb<sup>2+</sup> $f^{13}$  final states, where the former is derived from the Yb<sup>2+</sup> $f^{13}$   $J = 7/2$  final state, also known as the Kondo resonance peak, while the latter is the spin orbit split peak derived from the Yb<sup>2+</sup> $f^{13}$   $J = 5/2$  final state. Peaks marked with asterisks in Fig. 6 at binding energies 0.6 eV and 1.9 eV are corresponding surface core levels. The difference in binding energies between the bulk and surface doublets in our measurements is found to be  $\approx 0.6$  eV, consistent with earlier PES measurements.<sup>11,23</sup> Spectral

features observed at binding energies between 5 and 11 eV are derived from the Yb<sup>3+</sup> $f^{12}$  final states. Estimating the intensity of the photoemission peaks derived from Yb<sup>2+</sup> and Yb<sup>3+</sup> final states we obtain, in our thin films a mean Yb valence of  $2.78 \pm 0.06$  at 21 K. The Yb valence estimated from our thin films is consistent with earlier low energy photoemission (2.77 at 10 K)<sup>23</sup> and x-ray spectroscopy measurements (2.78 at 20 K),<sup>24,25</sup> but is higher than that estimated from soft x-ray PES (2.65 at 20 K).<sup>11</sup> Uncertainty in background subtraction leads to an uncertainty of  $\approx 4\%$  in our valence estimation, but our high energy resolution allows contributions from the surface states to be easily separated from that of the bulk states.

#### IV. CONCLUSION

In conclusion, we have demonstrated that epitaxial thin films of YbAl<sub>3</sub> (001) can be grown on MgO (001) by judicious choice of buffer layers and an optimized growth strategy. By providing access to pristine sample surfaces, our thin film approach could help elucidate microscopic mechanisms underlying the properties of YbAl<sub>3</sub> by directly measuring the single particle spectral function in both real and momentum space via surface spectroscopic probes such as ARPES and STM. Furthermore, our approach opens the possibility to engineer the properties of YbAl<sub>3</sub> and other mixed valence compounds via interfacial engineering or fabrication of heterostructures.

#### V. ACKNOWLEDGEMENTS

This work was supported by the National Science Foundation through DMR-0847385 and by the Cornell Center for Materials Research with funding from the NSF MRSEC program (DMR-1120296), and by the Research Corporation for Science Advancement (2002S). This work made use of the Cornell Center for Materials Research Shared Facilities which are supported through the NSF MRSEC program (DMR-1120296). The FEI Titan Themis 300 was acquired through NSF-MRI-1429155, with additional support from Cornell University, the Weill Institute, and the Kavli Institute at Cornell. S.C acknowledges helpful discussions with J.T. Heron and H.P. Nair.

<sup>1</sup>M. P. Allan, F. Massee, D. K. Morr, J. Van Dyke, A. W. Rost, A. P. Mackenzie, C. Petrovic, and J. C. Davis, Nat. Phys. 9,468 (2013).

<sup>2</sup>Y. F. Yang and D. Pines, Proc. Natl. Acad. Sci. U.S.A. 109, E3060 (2012).

<sup>3</sup>S. Chatterjee, J. Trinckauf, T. Hanke, D. E. Shai, J. W. Harter, T. J. Williams, G. M. Luke, K. M. Shen, and J. Geck, Phys. Rev. Lett. 110, 186401 (2013).

- <sup>4</sup>S. Kambe, H. Sakai, Y. Tokunaga, G. Lapertot, T. D. Matsuda, G. Knebel, J. Flouquet, and R. E. Walstedt, *Nat. Phys.* 10, 840 (2014).
- <sup>5</sup>H. Shishido, T. Shibauchi, K. Yasu, T. Kato, H. Kontani, T. Terashima, and Y. Matsuda, *Science* 327, 980 (2010).
- <sup>6</sup>Eryin Wang, Hao Ding, Alexei V. Fedorov, Wei Yao, Zhi Li, Yan-Feng Lv, Kun Zhao, Li-Guo Zhang, Zhijun Xu, John Schneeloch, Ruidan Zhong, Shuai-Hua Ji, Lili Wang, Ke He, Xucun Ma, Genda Gu, Hong Yao, Qi-Kun Xue, Xi Chen, and Shuyun Zhou, *Nat. Phys.* 9, 621 (2013).
- <sup>7</sup>M. Shimozawa, S.K. Goh, R. Endo, R. Kobayashi, T. Watashige, Y. Mizukami, H. Ikeda, H. Shishido, Y. Yanase, T. Terashima, T. Shibauchi, and Y. Matsuda, *Phys. Rev. Lett.* 112, 156404 (2014).
- <sup>8</sup>R.S. Kumar, A. Svane, G. Vaitheeswaran, V. Kanchana, E.D. Bauer, M. Hu, M.F. Nicol, and A.L. Cornelius, *Phys. Rev. B* 78, 075117 (2008).
- <sup>9</sup>A. Cornelius, J. Lawrence, T. Ebihara, P. Riseborough, C. Booth, M. Hundley, P. Pagliuso, J. Sarrao, J. Thompson, M. Jung, A. Lacerda, and G. Kwei, *Phys. Rev. Lett.* 88, 117201 (2002).
- <sup>10</sup>E. Bauer, C. Booth, J. Lawrence, M. Hundley, J. Sarrao, J. Thompson, P. Riseborough, and T. Ebihara, *Phys. Rev. B* 69, 125102 (2004).
- <sup>11</sup>S. Suga, A. Sekiyama, S. Imada, A. Shigemoto, A. Yamasaki, M. Tsunekawa, C. Dallera, L. Braicovich, T. L. Lee, O. Sakai, T. Ebihara, and Y. Onuki, *J. Phys. Soc. Jpn.* 74, 2880 (2005).
- <sup>12</sup>J. Yamaguchi, A. Sekiyama, S. Imada, A. Yamasaki, M. Tsunekawa, T. Muro, T. Ebihara, Y. Onuki, and S. Suga, *New J. Phys.* 9, 317 (2007).
- <sup>13</sup>P. Wahl, L. Diekhner, M. A. Schneider, F. Treubel, C. T. Lin, and K. Kern, *Phys. Rev. B* 84, 245131 (2011).
- <sup>14</sup>R. I. R. Blyth, J. J. Joyce, A. J. Arko, P. C. Canfield, A. B. Andrews, Z. Fisk, J. D. Thompson, R. J. Bartlett, P. Riseborough, J. Tang, and J. M. Lawrence, *Phys. Rev. B* 48, 9497 (1993).
- <sup>15</sup>B. D. Cullity, and S. R. Stock, *Elements of X-Ray Diffraction*, Prentice Hall, Upper Saddle River (2014), 315-326
- <sup>16</sup>001 diffraction peaks of YbAl<sub>3</sub> and LuAl<sub>3</sub> overlap, which makes it difficult to directly estimate the contribution from each layer. Intensity of the 001 diffraction peak of films with different LuAl<sub>3</sub> and YbAl<sub>3</sub> layer thicknesses was measured to confirm that both YbAl<sub>3</sub> and LuAl<sub>3</sub> layers are ordered.
- <sup>17</sup>Springer Materials Data Base, [http://materials.springer.com/isp/phase-diagram/docs/c\\_0902758](http://materials.springer.com/isp/phase-diagram/docs/c_0902758) and references therein.
- <sup>18</sup>S. Ohara, G. F. Chen, and I. Sakamoto, *J. Alloys and Compd.* 323, 632 (2001)
- <sup>19</sup>Z. Fisk, and M. B. Maple, *J. Alloys Compounds*, 183, 303 (1992)
- <sup>20</sup>T. Ebihara, S. Uji, C. Terakura, T. Terashima, E. Yamamoto, Y. Haga, Y. Inada, and Y. Onuki, *Physica B*, 281/282, 754 (2000)
- <sup>21</sup>K. Kadowaki, and S. B. Woods, *Solid State Commun.*, 58, 507 (1986)
- <sup>22</sup>N. Tsujii, H. Kontani, and K. Yoshimura, *Phys. Rev. Lett.*, 94, 057201 (2005)
- <sup>23</sup>L.H. Tjeng, S.-J. Oh, E. -J. Cho, H. -J. Lin, C. T. Chen, G. -H. Gweon, J. -H. Park, J. W. Allen, T. Suzuki, M. S. Makivic, and D.L. Cox, *Phys. Rev. Lett.*, 71, 1419 (1993)
- <sup>24</sup>J. M. Lawrence, G. H. Kwei, P. C. Canfield, J. G. DeWitt, and A.C. Lawson, *Phys. Rev. B* 49, 1627 (1994)
- <sup>25</sup>L. Moreschini, C. Dallera, J. J. Joyce, J. L. Sarrao, E. D. Bauer, V. Fritsch, S. Bobev, E. Carpene, S. Huotari, G. Vanko, G. Monaco, P. Lacovig, G. Panaccione, A. Fondacaro, G. Paolicelli, P. Torelli, and M. Grioni, *Phys. Rev. B* 75, 035113 (2007)

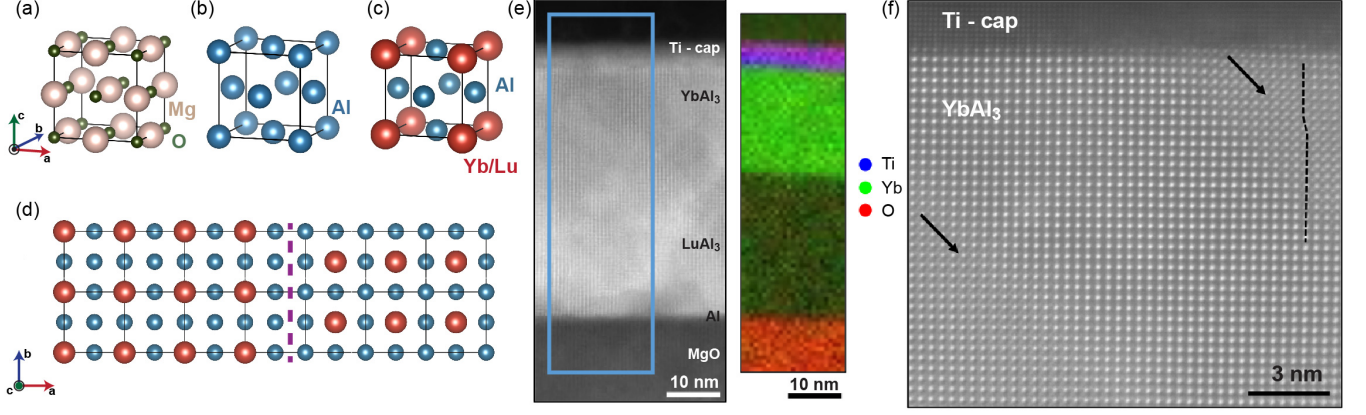


FIG. 1. Crystal structure of (a) MgO, (b) Al, and (c) YbAl<sub>3</sub>/LuAl<sub>3</sub>. (d) Illustration of two possible domains of YbAl<sub>3</sub>/LuAl<sub>3</sub> on Al when viewed along the [001] direction and an anti-phase domain boundary (violet dotted line) between them. (e) High resolution high angle annular dark field scanning transmission electron microscopy (HAADF-STEM) image and elemental map of a 20 nm thick YbAl<sub>3</sub> film grown on 30 nm thick LuAl<sub>3</sub> and 1.2 nm Al buffer layers. The film is capped by 6 nm of Ti to protect the film from oxidation. EELS mapping was performed in the area marked in blue. (f) HAADF-STEM image showing the atomic arrangement of Yb atoms in the YbAl<sub>3</sub> film. Anti-phase domain boundaries are highlighted with black arrows. Dotted black line shows the shift of Yb atomic positions by  $(\frac{1}{2}, \frac{1}{2}, 0)$  across an anti-phase domain boundary.

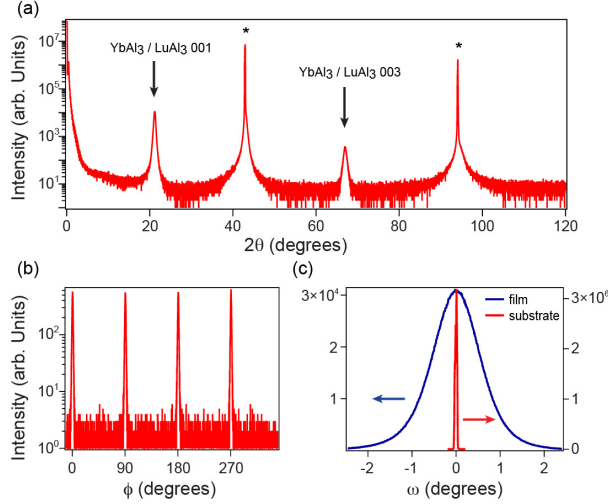


FIG. 2. (a) Out-of-plane  $\theta$ -2 $\theta$  scan of a film with identical composition as in Fig. 1(e) and (f) but without a Ti capping layer. 001 and 003 peaks of the ordered L12 structure (shown in Fig. 1 (c)) establish that the film is ordered. Substrate peaks are marked by asterisks. (b) Azimuthal  $\phi$  scan of the 101 YbAl<sub>3</sub> diffraction peak at  $\chi = 45^\circ$ , where  $\chi = 0^\circ$  aligns the diffraction vector perpendicular to the plane of the substrate.  $\phi = 0^\circ$  corresponds to the in-plane component of the diffraction vector aligned parallel to the [100] direction of the (001) MgO substrate. The  $\phi$  scan in (b) establishes the epitaxial relationship to be (001)[100] YbAl<sub>3</sub> || (001)[100] MgO. (c) Rocking curve comparison between the 001 film peak and 002 substrate peak.

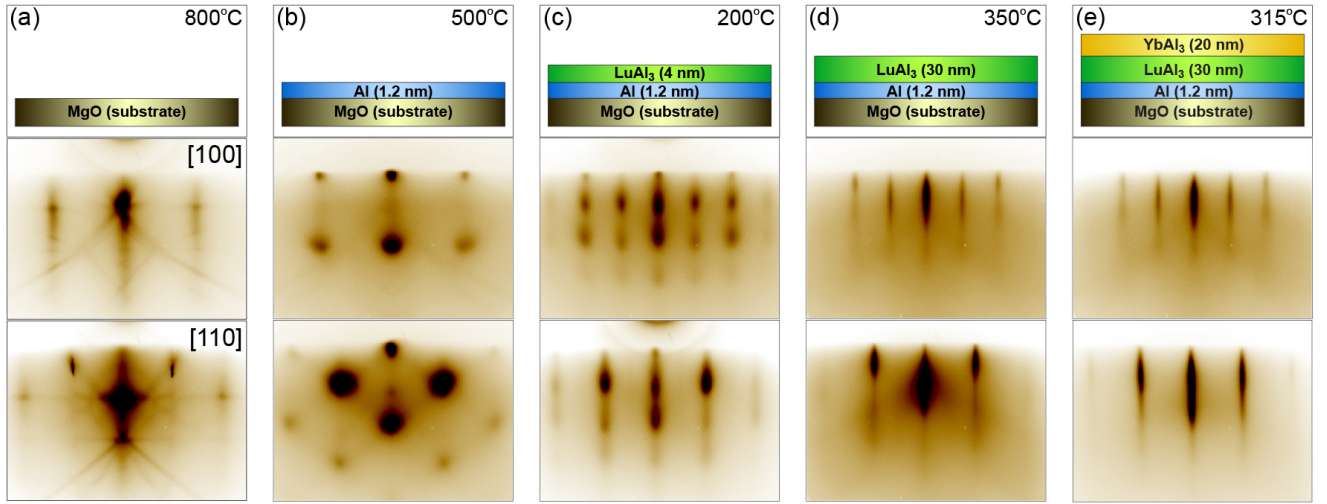


FIG. 3. RHEED images at different stages of the growth of a YbAl<sub>3</sub>/LuAl<sub>3</sub>/Al/MgO heterostructure. (a)-(e) Schematics of the layers present in the thin film heterostructure at each stage of growth at which RHEED patterns were recorded. Substrate temperatures are noted in the top right corner of the top panel. Corresponding RHEED spectra along the [100] and [110] azimuths are in the middle and the bottom panels, respectively.

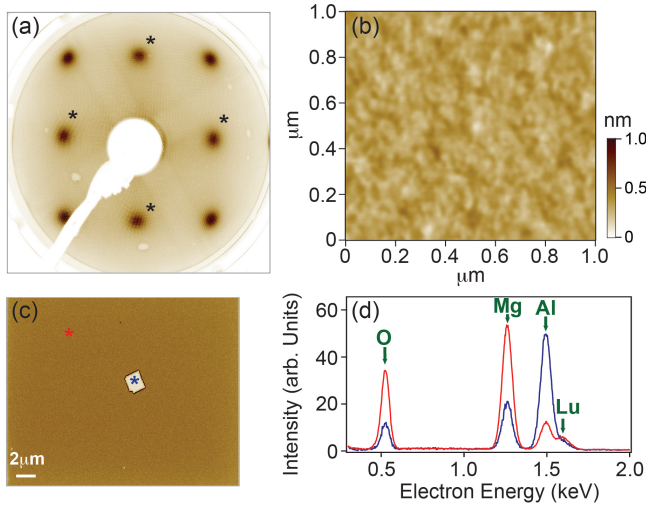


FIG. 4. (a) LEED image taken on a 20 nm thick uncapped YbAl<sub>3</sub> film. Diffraction peaks with mixed indices are marked by asterisks. (b) AFM image of the same film. The measured rms surface roughness is  $\approx 0.18$  nm. (c) SEM image of a 35 nm thick LuAl<sub>3</sub> film corroborating the smoothness of the films over a large area. (d) EDX scans taken in regions marked by asterisks in (c).

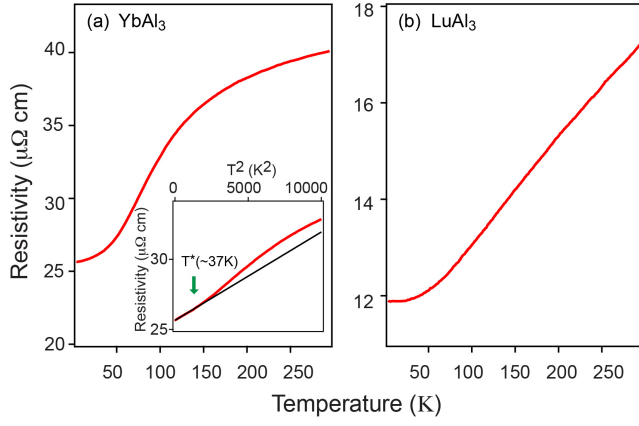


FIG. 5. Temperature-dependent resistivity of (a) 20 nm YbAl<sub>3</sub>/ 1.6 nm LuAl<sub>3</sub>/ 1.2 nm Al and of (b) 35 nm LuAl<sub>3</sub>/ 1.2 nm Al. Inset in (a) shows the onset of coherence at  $\approx 37$  K in the 20 nm thick YbAl<sub>3</sub> film above which the resistivity starts to deviate from  $T^2$  behavior. (black line)

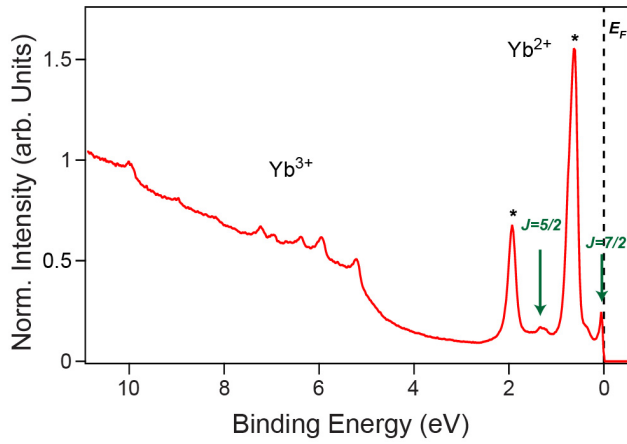


FIG. 6. PES spectra of YbAl<sub>3</sub> obtained at 21 K. Peaks between 5 eV and 11 eV binding energy are derived from the Yb<sup>3+</sup> $f^{12}$  final state while those between 0 eV and 3 eV binding energy are derived from the Yb<sup>2+</sup> $f^{13}$  final state. The  $J = 7/2$  and  $J = 5/2$  spin orbit split states are indicated by arrows, whereas peaks marked with asterisks are the corresponding surface core level shifts.